Effect of pre-strain and excess length on unsteady fluid-structure interactions of membrane airfoils

P. Rojratsirikul, Z. Wang and I. Gursul*

Department of Mechanical Engineering

University of Bath, Bath BA2 7AY, United Kingdom

Aerodynamic characteristics of two-dimensional membrane airfoils were experimentally investigated in a wind tunnel. The effects of the membrane pre-strain and excess length on the unsteady aspects of the fluid-structure interaction were studied. The deformation of the membrane as a function of angle of attack and free stream velocity was measured using a high-speed camera. These measurements were complemented by the measurements of unsteady velocity field with a high frame rate Particle Image Velocimetry (PIV) system as well as smoke visualization. Membrane airfoils with excess-length exhibit higher vibration modes, earlier roll-up of vortices, and smaller separated flow regions, whereas the membranes with pre-strain generally behave more similarly to a rigid airfoil. Measured frequencies of the membrane vibrations suggest a possible coupling with the wake instabilities at high incidences for all airfoils.

* Corresponding author. E-mail address: i.a.gursul@bath.ac.uk.

Nomenclature

c = airfoil chord length

c_e = effective length of the membrane

C_t = tension coefficient, $\overline{T}/q_\infty c$

E = Young's modulus

f = frequency

L_0 = initial membrane length

$\overline{L}$ = time-averaged membrane length

q_∞ = dynamic pressure, $\frac{1}{2}\rho U_\infty^2$

Re = Reynolds number, $\rho U_\infty c/\mu$

S_0 = pre-stress, $E\delta_0$

St = Strouhal number

$\overline{T}$ = time-averaged tension, $(S_0+E\overline{\delta})t$

t = membrane thickness

u' = fluctuating velocity in the streamwise direction

U_∞ = free stream velocity

V = magnitude of velocity vector

v' = fluctuating velocity in the cross-stream direction

z = camber

z_{max} = maximum camber

z_{SDmax} = maximum standard deviation of membrane displacement

α = angle of attack

$\overline{\delta}$ = time-averaged strain

δ_0 = pre-strain

ε = excess length ratio, $(L_0 - c_e)/c_e$

μ = viscosity of air

Π_1 = aeroelastic parameter, $(Et/q_\infty c)^{1/3}$

ρ = density of air

ρ_m = density of membrane

1. Introduction

Flexible membrane wings have been associated with a number of applications including either man-made vehicles such as parachutes, paragliders, hang gliders, yacht sails, microlights, and Micro Air Vehicles (MAVs), or natural flyers such as bats. For MAV applications in general, where the vehicles operate at Reynolds numbers below 10^5, poor lift and unsteadiness represent major problems in low Reynolds number aerodynamics. It is highly desirable to design MAVs that are able to operate under wind gust and unsteady free stream conditions. Several studies have shown that membrane wings can significantly improve longitudinal static stability, delay stall and provide more favorable lift-to-drag ratio, and therefore enhance the overall aerodynamic performance when compared to a rigid wing of similar geometry due to its desirable aeroelastic effects and the adaptive inflation of the membrane skin (Shyy et al., 1997; 1999; Ifju et al., 2002; Lian et al., 2003; Lian and Shyy, 2003; Albertani et al., 2007).

The study of membrane wings for MAV applications has been partly motivated by observations of bats. These mammals hunt for insects, therefore they must have high

agility (rate at which a turn can be initiated) and good maneuverability (minimum space for a turn at a given speed) (Norberg and Rayner, 1987). During the insect capture, some bat species perform rapid turns, rolls, dives, and climbs, whereas other species fly slowly and hover close to vegetation, yet other bat species commute over substantial distances, hence they must be capable of sustained steady flight. These astonishing flight performances of bats can be attributed to their exceptional membrane wing structure, which has recently been an inspiration for micro air vehicle designs.

In computational approaches, the potential flow theory (Newman and Low, 1984; Newman, 1987; Greenhalgh et al., 1984; Jackson and Christie, 1987), laminar flow (Smith and Shyy, 1995), and turbulent flow (Smith and Shyy, 1996) were used to simulate the membrane shape in equilibrium in steady conditions. It was found that the potential flow theory can only be sufficient for inextensible membranes with small camber and incidence, as there is no flow separation. Unsteady aspects of the fluid-structure interaction have received less attention. The study by Galvao et al. (2006) on a low aspect ratio (AR=0.92) membrane wing reported that standing waves with large mode number were observed. Similar vibrational modes were presented for a rectangular wing with AR=1.38 in a subsequent study by Song and Breuer (2007). Force measurements were presented together with the deformation data by Song et al. (2008). The flow is highly three-dimensional and tip vortices are dominant for low aspect ratio wings. It is possible that the membrane vibrations can excite the separated shear layer forming the tip vortices and promote reattachment (Gursul et al., 2005). For a flexible nonslender delta wing, this mechanism delays the stall and increases the lift (Taylor et al.,

2007). Hence, the unsteady fluid-structure interactions of low aspect ratio wings are expected to be strongly affected by the tip/leading-edge vortices.

Unsteady fluid-structure interactions of membrane airfoils at low Reynolds numbers have been recently studied experimentally (Rojratsirikul et al., 2008; 2009a) and computationally (Gordnier, 2008; Gordnier and Attar, 2009; Matthews et al., 2008). In our previous study (Rojratsirikul et al., 2009a) we investigated two-dimensional flexible membrane airfoils with zero pre-tension with particular emphasis on the unsteady aspects of the fluid-structure interaction at low Reynolds numbers. It was found that the amplitude and mode of the membrane vibrations depend mainly on the relative location and magnitude of the unsteadiness of the separated shear layer. The results indicated strong coupling of membrane oscillations with the unsteady flow, in particular with vortex shedding in the wake. Comparison of rigid (but cambered) and flexible membrane airfoils shows that the flexibility delays the stall. Hence this is a potential passive flow control method using flexibility in nature and engineering applications.

In this article, we extend our previous work to the effect of membrane pre-strain and excess length on the unsteady aspects of the fluid-structure interaction. Measurements of the membrane deformation and time-accurate velocity field as well as smoke visualization were conducted as a function of angle of attack and free-stream velocity. The effects of pre-strain and excess length were investigated in detail. Comparisons with the previous results for the airfoil with zero pre-tension were made.

2. Experimental Setup and Procedures

2.1. Models

The experiments were carried out in the low-speed, closed-loop open-jet wind tunnel with the circular working section of 760 mm in diameter, located in the Department of Mechanical Engineering, University of Bath. The details of the setup are similar to those of the previous work (Rojratsirikul et al., 2008; 2009a). The membrane airfoil was placed in the test section by means of a frame and end plates as shown in Fig. 1(a). Both the leading-edge and trailing-edge of the wing were fixed to circular plates at both ends to adjust the angle of attack. The rigid leading- and trailing-edges run along the whole span of the test section between the two end plates with a small gap (1 mm) between the membrane and the end plates. The membrane deformation appeared uniform in the spanwise direction in visual inspections. In the preliminary experiments, the time-averaged deformation was measured near the tip region (near the end plates) and the difference was found to be less than 10% of the values at the mid-span plane. The airfoil had a span of 450 mm and chord length of c = 150 mm. The experiments were carried out over angles of attack α from 0 to 30 degrees, free stream velocities U_∞ of 5, 7.5, and 10 m/s which correspond to Reynolds numbers, based on the chord length, of Re = 53 100, 79 700 and 106 000 respectively.

The membrane airfoil was made from a black latex rubber sheet with thickness t = 0.2 mm, Young's modulus E = 2.2 MPa, and density of membrane ρ_m = 1 gr/cm^3. The membrane's modulus of elasticity was measured by subjecting the membrane to known tension and measuring the strain with a high resolution digital camera. In these

experiments, the strain was varied up to 6% and both the new and used membranes were tested. It was found that the tension-strain relation is linear in this range. The membrane airfoils with different initial strains of $\delta_0 = 2.5\%$, $\delta_0 = 5\%$ and excess lengths of $\varepsilon = 2.5\%$, $\varepsilon = 5\%$ were made from the same material. The uncertainty of the pre-strain or excess length of the airfoils is estimated as $\Delta\delta_0 = \Delta\varepsilon = 0.5\%$. Each membrane was attached to the airfoil-shaped leading- and trailing-edges as shown in Fig. 1(b), resulting in an effective length of the membrane, $c_e = 137$ mm. The aeroelastic parameter used by Smith and Shyy (1996) has values of $\Pi_1 = 5.77$, 4.41, and 3.64 based on $U_\infty = 5$, 7.5, and 10 m/s respectively. In addition, a rigid airfoil made of 1 mm thick steel plate with a shape equivalent to the mean membrane deformation was tested in order to reveal the effects of membrane vibrations (Rojratsirikul et al., 2008; 2009a).

2.2. Measurements of deformation

In order to measure the membrane shape, a thin laser sheet from a 4W Argon-Ion laser was used to illuminate the membrane surface in the streamwise plane located at the mid-span of the wing. A high speed camera (Photron FASTCAM APX) was positioned normal to the flow and images were captured at a rate of 1500 frames per second. The resulting image appears as a white curve as shown by the example in Fig. 2. The images with 1024×1024 pixel resolution in TIF format were obtained in 2 seconds, resulting in 3000 images per each angle of attack and speed. Finally, the images were digitized through MatLab (Image Processing Toolbox) to find the coordinates. The uncertainty of the measurements of the membrane displacement with the present technique is estimated as $\Delta z/c$=0.1%. Examples of the digitized membrane shapes at different instants are shown

in Fig. 3. Different modes of vibrations (second, fourth and fifth modes) are seen in these examples. This technique can only detect the chordwise modes. Although the time-averaged deformation is nearly uniform in the spanwise direction, this does not rule out possible existence of the spanwise modes, which can not be detected with the present technique.

From the instantaneous coordinates of the membrane, the time-averaged membrane shape was calculated for each angle of attack and free stream velocity. The time-averaged strain, $\overline{\delta}$, was then calculated from the mean shape:

$$\overline{\delta} = (\overline{L} - L_0) / L_0 , \tag{1}$$

where $\overline{L}$ is the time-averaged membrane length, and L_0 is the initial membrane length. The tension coefficient C_t was calculated using the definition of

$$C_t = \overline{T} / q_\infty c , \tag{2}$$

where

$$\overline{T} = (S_0 + E\overline{\delta})t , \tag{3}$$

in which $\overline{T}$ is the time-averaged tension, q_∞ is the dynamic pressure, and S_0 is the pre-stress ($S_0 = E\delta_0$).

From the digitized membrane shapes as a function of time, it was also possible to study the time history of the displacement. The dominant frequencies were found by the spectral analysis using the Fast Fourier Transform (FFT) method in MatLab.

2.3. Velocity measurements

Quantitative flow measurements were undertaken using a high frame-rate Digital Particle Image Velocimetry (DPIV) system. Illumination of the desired plane was achieved using a New Wave Pegasus Nd:YLF double pulse high speed laser with a maximum energy of 10 mJ per pulse. The laser light sheet was placed parallel to the free stream velocity to illuminate a plane at the mid-span of the wing as shown in Fig. 1(a). The PIV camera was placed normal to the flow, and the flow over the suction surface of the whole wing was imaged. In some experiments, specific areas near the leading-edge or trailing-edge were investigated. The images were captured using a TSI PowerView HS-3000 high speed CMOS camera. A TSI LaserPulse synchronizer unit was utilized to link the camera and the laser to enable the accurate capture of images for two frame cross-correlation analysis. For these measurements, the velocity field was captured at a rate of 1,500 frames per second, at a resolution of 1024 by 1024 pixels, producing sequences of 3,000 instantaneous velocity fields over 2 seconds. A TSI model 9307-6 multi-jet atomizer was used to produce oil droplets in order to seed the flow. The atomizer worked best using olive oil and the mean size of the droplets was 1μm. The commercial software TSI Insight3G and a FFT cross-correlation algorithm were used for the analysis of the results obtained. The size of the interrogation window was 20 by 20 pixels, resulting in an effective grid size around 2% of the chord length in these measurements. The measurement uncertainty for the velocity is estimated as 2% of the free stream velocity.

2.4. Smoke flow visualization

Flow visualization was performed using a smoke wire. In order to generate smoke, a strip

of wire was clamped vertically, perpendicular to the flow upstream of the wing and at the mid-span. Oil was dropped to the wire continuously by a small valve on a dripping system. With a current applied to the wire, the oil was burnt by the heat, and the smoke was generated. A high speed camera (Photron FASTCAM APX) was used to capture images at a rate of 1 000 frames per second.

3. Results

3.1. Mean shape of membrane

Figure 4 shows the maximum camber of the time-averaged membrane shape for different membrane pre-strains and excess lengths as a function of angle of attack at different free stream velocities. Note that the smallest angle of attack shown for a given airfoil corresponds to the onset of the bistable instability. For the lowest free stream velocity U_∞ = 5 m/s, the maximum camber increases gradually up to a moderate incidence, then stays roughly constant for the airfoils with nonzero pre-strains. For zero pre-strain and excess length cases, the changes in maximum camber are small as the angle of attack is varied, which is consistent with our previous observations (Rojratsirikul et al., 2008; 2009a) and simulations by Gordnier (2008). As expected, the largest maximum camber is observed for the airfoils with excess length. However, the difference between the two airfoils with different excess length appears to be small. With increasing free stream velocity to U_∞ = 7.5 m/s and 10 m/s, the maximum camber increases for all airfoils. The observations are very similar for all speeds. Although not shown here, the location of the maximum camber is at about the mid-chord point for small incidences. It tends to move forward as the angle of attack increases up to a certain incidence, and tends to move back at higher

angles of attack. The location of the maximum camber is only slightly sensitive to the membrane pre-strain and excess length ratio. Similarly, previous experiments (Rojratsirikul et al., 2008; 2009a) showed that the location of the maximum camber is not very sensitive to the free stream velocity.

The time averaged strain is shown in Fig. 5. The airfoils with excess length show larger time-averaged strain than the airfoils with pre-strain at higher free stream velocities. This is particularly obvious at the highest free stream velocity, U_∞ = 10 m/s. The strain rate is very similar for airfoils with δ_0 = 0%, ε = 2.5% and 5%. The strain increases with the free stream velocity for all airfoils, but the rate of increase of strain with free stream velocity is larger for the airfoils with δ_0 = 0%, ε = 2.5% and 5%.

These three different free-stream velocities also represent three different regimes for the membrane tension. As the membrane tension is proportional to the total strain, $\overline{T} = E(\delta_0 + \delta)t$, it is seen that, for U_∞ = 5 m/s, the tension is dominated by the pre-strain. The membrane tension is much larger for δ_0 = 2.5% and 5% compared to other cases. With increasing free stream velocity to U_∞ = 7.5 m/s, the airfoils with no pre-strain show a large increase in tension, although the tension is still larger for those with pre-strain. Eventually, at the largest free stream velocity U_∞ = 10 m/s, the membrane tension reaches similar levels for all cases. In terms of the tension coefficient, it decreases with increasing free-stream velocity (Rojratsirikul et al., 2009b).

3.2. Mean flow

Figure 6 shows the magnitude of the time-averaged velocity and streamlines for different airfoils with pre-strain and excess length. Note that the flow is from right to left. In this figure, for each airfoil, the mean flow is shown for $\alpha = 12°$ (left column) and $\alpha = 20°$ (right column). For the lowest free stream velocity, $U_\infty = 5$ m/s, it is shown that the shear layer gets closer to the membrane surface and separation is delayed as the camber of the airfoil increases due to the excess length. For $\delta_0 = 0\%$ and $\alpha = 12°$, even though the separation takes place at the leading-edge, the shear layer remains close to the membrane surface. For nonzero pre-strain, the shear layer moves away from the surface as the separation region becomes larger. In summary, the airfoils with pre-strain have large flow separation region, whereas the airfoils with excess length, hence large camber, exhibit small separated regions. For all airfoils, comparison of left and right columns shows that the separation region becomes larger at $\alpha = 20^o$, as expected.

Figure 7 shows a comparison of the mean flow for $U_\infty = 5$ m/s (left column) and $U_\infty = 7.5$ m/s (right column) for various airfoils with pre-tension and excess length. For the angle of attack $\alpha = 20^o$, the airfoils at the larger free stream velocity ($U_\infty = 7.5$ m/s) exhibit larger cambers and smaller separated regions. This is also consistent with the previous results (Rojratsirikul et al., 2008; 2009a) which reported the trend of shear layer getting closer to the wing surface as the camber of the wing increases.

3.3. Membrane oscillations

Figure 8 summarizes various regimes based on the observations of the membrane oscillations for different airfoils with pre-strain and excess length. In the steady regime, where membrane oscillations are insignificant, the flow remains attached for small incidences. In some cases, such a steady regime was also observed at high angles of attack, which is likely to be due to the shear layer being far away from the membrane. In the unsteady regime, membrane oscillations are significant, and corresponding vibration modes and frequencies can be easily detected. In the bistable regime, which is observed for small angles of attack near zero, the bistable instability (luffing) occurs and the membrane can easily switch from positive to negative camber (Newman and Paidoussis, 1991). It is seen in Fig. 8 that the bistable regime is more dominant for airfoils with excess length. The onset of the membrane vibrations also occurs at a slightly larger angle of attack for airfoils with excess length.

Figures 9-13 show the power spectral density of the membrane displacement (for the chordwise location where the standard deviation of the displacement is maximum) as a function of Strouhal numbers, fc/U_∞, and angle of attack for $\delta_0 = 5\%$, $\delta_0 = 2.5\%$, $\delta_0 = 0\%$, $\varepsilon = 2.5\%$ and $\varepsilon = 5\%$ respectively. These plots show the frequencies at which large amplitude of vibrations (shown with the dark shades) take place for each incidence. In general, airfoils with excess length or zero pre-strain have larger amplitude oscillations compared to the airfoils with nonzero pre-strain. It is seen that the vibration occurs at certain modes. For each airfoil, the vibration modes were identified from the time variation of the membrane shape such as those shown in Figure 3. The mode numbers were confirmed from these graphs, or by calculating the standard deviation of the

membrane displacement and counting the peaks. Figures 9-13 show that the airfoils with pre-strain exhibit the first and second modes predominantly. The airfoils with excess length tend to have higher mode numbers than those with pre-strain at all incidences. For all free stream velocities and all airfoils, there are certain incidences where there are jumps in the dominant mode. In particular, a change to the second mode at high incidences is observed.

The general trend for airfoils with zero or excess length is that the higher modes are observed at moderate incidences ($\alpha \geq 10°$) when noticeable oscillations start. The separation is typically delayed for these airfoils (see Fig. 6 for $\alpha = 12°$). It is likely that the membrane vibrations couple with the most unstable frequencies of the shear layer. Although the natural frequency of the shear layer instabilities for rigid airfoils was not measured in this investigation, we expect that the natural frequency of the separated shear layer is higher than the shedding frequency in the wake. Wu et al. (1998) estimates that the ratio of the shear layer frequency to the wake shedding frequency is 6.6 for NACA 0012, which provides an estimate of $fc/U_\infty \cong 2.5$ for this airfoil. In the present investigation, we obtain $fc/U_\infty = 2$ to 3, if the same ratio of the frequencies is used. On the other hand, at higher angles of attack, flows are typically separated at the leading-edge (see Fig. 6 for $\alpha = 20°$) and the membrane appears to couple with the wake instabilities as will be discussed further later on.

An attempt was made to predict the natural frequencies of the membrane based on the linear elastic theory, using the estimated tension from the mean deformation. Assuming

two-dimensional membrane shape, our predictions for the first mode varied between ±100% of the experimentally measured frequencies, depending on the free stream velocity, pre-strain or excess length, with no clear trend. We believe that this highlights the nonlinear nature of the fluid-structure interaction. In general, the Strouhal number is on the order of unity. At relatively high angles of attack, where the second mode is always observed, the Strouhal number is close to unity regardless of the pre-strains and excess lengths of the membrane. This is consistent with previous results (Rojratsirikul et al., 2008, 2009a), suggesting a coupling of the membrane oscillations with vortex shedding from the membrane. An alternative definition of the Strouhal number, based on the vertical distance between the leading-edge and trailing-edge, is often used in the literature (Fage and Johansen, 1927; Abernathy, 1962):

$$\mathrm{St}_{\alpha} = \frac{fc\sin\alpha}{U_{\infty}}. \tag{4}$$

This modified definition of the Strouhal number is reported to be constant for flat plates and thin airfoils, with values given in the range of 0.16 to 0.22 (Fage and Johansen, 1927; Abernathy, 1962; Miranda et al., 2005). In this study, the vortex shedding frequency in the wake of a rigid membrane (an equivalent rigid cambered airfoil which was used in previous investigation) was obtained with hot-wire anemometry and is shown in Fig. 9-13. The uncertainty of the measurements of the vortex shedding frequency with hot-wire anemometry was estimated as 3%. We have not measured the natural wake frequencies for a range of camber values, and the rigid thin airfoil had a shape derived from the zero pre-strain membrane only. It represents an average of the cases with smaller camber (airfoils with pre-strain) and larger camber (airfoils with excess length). Nevertheless, the constant for the modified Strouhal number is expected to be not too different, as it is

around 0.2 for various bluff bodies. In these figures, the symbols show the measured frequencies in the wake and the dashed line shows the variation of the Strouhal number calculated from the alternative definition based on the vertical distance between the leading-edge and trailing-edge, assuming a constant value of 0.17 to fit our data. The results suggest that the membrane oscillations might be coupled with the vortex shedding. In particular, at high incidences where the second mode is observed, the membrane oscillations might be coupled with the first harmonic of the natural frequency. In active flow control studies with rigid airfoils by Miranda et al. (2005) and Wu et al. (1998), it was found that vortex shedding may lock on the first harmonic or the subharmonic of the natural frequency.

3.4. Unsteady flow

Figure 14 shows the comparison of the turbulence intensity $\overline{u'^2+v'^2}/U_\infty^2$ in the measurement plane for the airfoils with excess length of 2.5%, 5%, and pre-strain 2.5%, 5%, together with the results of the airfoil with zero pre-strain at α = 14^o (left column), 18^o (middle column) and 25^o (right column), for U_∞ = 5 m/s. For α = 14^o, the weakest shear layer fluctuations are seen for the airfoil with excess length, whereas the strongest turbulence intensity is observed for the membrane with pre-tension. With increasing angle of attack, the shear layer moves away from the membrane surface. For airfoils with excess length, the turbulence intensity increases with increasing angle of attack. For other airfoils, there is a decrease in turbulence intensity with increasing incidence.

The Reynolds stress component shown in Fig. 15 exhibits similar trend to that of the turbulence intensity. The location of the maximum values of the Reynolds stress moves away from the membrane surface and downstream with increasing angle of attack. Peak magnitudes are observed for the airfoil with 2.5% pre-strain at α = 14° and 18°, and for the airfoil with 5% excess length at α = 20°. The relatively large value of the Reynolds stress observed for these cases is related to the formation of coherent structures. Examinations of the instantaneous flow fields suggest that the peak of the Reynolds stress coincides with the roll-up of the large vortices.

3.5. Smoke flow visualization

The smoke flow patterns for 2.5% excess length ratio and 2.5% pre-tension together with the results for the airfoil with zero pre-tension and the rigid airfoil are presented in Fig. 16. It is seen that at the lower incidence ($\alpha = 14^o$), the size of the separation region for ε = 2.5% and δ = 0% is small. The oscillation of the membrane with excess length seems to excite the shear layer. The airfoil with pre-tension shows a larger size of separation region than the one with zero pre-tension, and this is more evident at the higher incidence. At the higher incidence ($\alpha = 18^o$) the roll-up of large vortices is evident over the flexible membrane with ε = 2.5% and δ = 0%. The membrane airfoil with ε = 2.5% shows the smallest size of separation region among other airfoils. The airfoil with pre-tension does not induce the roll-up of vortices over the airfoil. This is also similar to the flow pattern for the rigid airfoil.

4. Conclusions

High frame rate measurements of deformation and velocity fields were conducted for various membrane airfoils with pre-strain and excess length. The maximum camber and strain of the time-averaged membrane depends on the membrane pre-strain and excess length. The effect of the angle of attack is small for these mostly separated flows at low Reynolds numbers. The largest camber is observed for the airfoil with excess length. The strain is also largest for the airfoil with excess length. The membrane tension is dominated by the pre-tension at the smallest free-stream velocity, but it becomes of similar magnitude for all airfoils with increasing free stream dynamic pressure. The time-averaged velocity field exhibits smaller separated region for airfoils with excess length due to their larger camber. The shear layer moves closer to the airfoil surface and separation is delayed with increasing free stream velocity. On the other hand, the airfoils with pre-strain have large flow separation regions.

The onset of the membrane vibrations is delayed to a larger angle of attack for the airfoils with excess length. In general, the mode number of the membrane vibrations is larger for the membranes with excess-length than for those with pre-strain. Mode numbers up to six are observed, and the Strouhal number remains on the order of unity. Both the mode number and Strouhal number tend to decrease with increasing angle of attack. Measured frequencies of the membrane vibrations suggest a possible coupling with the wake instabilities. The magnitude of the shear layer fluctuations is seen to be dependent on the angles of attack, and the trends are different for the airfoils with excess length and pre-strain. The Reynolds stress component shows a similar trend to that of the turbulence

intensity. The roll-up of large vortices excited by the membrane oscillations at high angle of attack is more evident, and the shear layer is closer to the airfoil surface for the airfoil with excess length than for the one with pre-tension, which generally behaves more similarly to a rigid airfoil.

Acknowledgments

The authors would like to acknowledge funding from the US Air Force Office of Scientific Research (AFOSR) under grant number FA8655-07-1-3044, the Research Councils UK Academic Fellowship in Unmanned Air Vehicles, and the Royal Thai Government Scholarship. The authors would like to thank the EPSRC Engineering Instrument Pool.

References

Abernathy, F.H., 1962. Flow over an inclined plate. ASME Journal of Basic Engineering 84, 380-388.

Albertani, R., Stanford, B., Hubner J. P., and Ifju, P. G., 2007. Aerodynamic coefficients and deformation measurements on flexible micro air vehicle wings. Experimental Mechanics 47, 625-635.

Fage, A., and Johansen, F.C., 1927. On the flow of air behind an inclined flat plate of infinite span. In: Proceedings of The Royal Society, London, England, Series A, Vol. 116, pp. 170-197.

Galvao, R., Israeli, E., Song, A., Tian, X., Bishop, K., Swartz, S., and Breuer, K., 2006. The aerodynamics of compliant membrane wings modeled on mammalian flight mechanics. In: Proceedings of the 36th AIAA Fluid Dynamics Conference and Exhibit, Jun. 2006, San Francisco, AIAA 2006-2866.

Gordnier, R.E., 2008. High fidelity computational simulation of a membrane wing airfoil. In: Proceedings of the 46th AIAA Aerospace Sciences Meeting and Exhibit, 7-10 Jan. 2008, Reno, Nevada, AIAA 2008-614. See also, Journal of Fluids and Structures, in press.

Gordnier, R.E., and Attar, P.J., 2009. Implicit LES simulations of a low Reynolds number flexible membrane wing airfoil. In: Proceedings of the 47th AIAA Aerospace Sciences Meeting and Exhibit, 5-8 Jan. 2009, Orlando, Florida, AIAA 2009-0579.

Greenhalgh, S., Curtiss, H.C., and Smith, B., 1984. Aerodynamic properties of a two-dimensional inextensible flexible airfoil. AIAA Journal 22, 865-870.

Gursul, I., Gordnier, R., and Visbal, M., 2005. Unsteady aerodynamics of nonslender delta wings. Progress in Aerospace Sciences 41, 515-557.

Ifju, P. G., Jenkins, D.A., Ettinger, S., Lian, Y., and Shyy, W., 2002. Flexible-wing-based micro air vehicles. In: Proceedings of the 40th AIAA Aerospace Sciences Meeting and Exhibit, Jan. 2002, Reno, Nevada, AIAA 2002-0705.

Jackson, P.S., and Christie, G.W., 1987. Numerical analysis of three-dimensional elastic membrane wings. AIAA Journal 25, 676-682.

Lian, Y., and Shyy, W., 2003. Three-dimensional fluid-structure interactions of a membrane wing for micro air vehicle applications. In: Proceedings of the 44th AIAA/ASME/ASCE/AHS Structures, Structural Dynamics, and Materials Conferences, 7-10 Aprl. 2003, Norfolk, VA. AIAA 2003-1726.

Lian, Y., Shyy, W., and Haftka, R., 2003. Shape optimization of a membrane wing for micro air vehicles. In: Proceedings of the 41thAIAA Aerospace Sciences Meeting and Exhibit, 6-9 Jan. 2003, Reno, Nevada, AIAA 2003-0106.

Matthews, L.A., Greaves, D.M., and Williams, C.J.K., 2008. Numerical simulation of viscous flow interaction with an elastic membrane. International Journal For Numerical Methods in Fluids 57, 1577-1602.

Miranda, S., Vlachos, P.P., Telionis, D.P., and Zeiger, M.D., 2005. Flow control of a sharp-edged airfoil. AIAA Journal 43, 716-726.

Newman, B.G., 1987. Aerodynamic theory for membranes and sails. Progress in Aerospace Sciences 24, 1-27.

Newman, B.G., and Low, H.T., 1984. Two-dimensional impervious sails: experimental results compared with theory. Journal of Fluid Mechanics 144, 445-462.

Newman, B.G., and Paidoussis, M.P., 1991. The stability of two-dimensional membranes in streaming flow. Journal of Fluids and Structures 5, 443-454.

Norberg, U. M., and Rayner, J. M. V., 1987. Ecological morphology and flight in bats (mammalian; chiroptera): wing adaptations, flight performance, foraging strategy and echolocation. Philosophical Transactions of the Royal Society of London, Series B, Biological Sciences, 316, 335-427.

Rojratsirikul, P., Wang, Z., and Gursul, I., 2008. Unsteady aerodynamics of membrane airfoils. In: Proceedings of the 46th AIAA Aerospace Sciences Meeting and Exhibit, 7-10 Jan. 2008, Reno, Nevada, AIAA 2008-613.

Rojratsirikul, P., Wang, Z., and Gursul, I., 2009a. Unsteady fluid-structure interactions of membrane airfoils at low Reynolds numbers. Experiments in Fluids 46, 859-872.

Rojratsirikul, P., Wang, Z., and Gursul, I., 2009b. Effect of pre-strain and excess length on unsteady fluid-structure interactions of membrane airfoils. In: Proceedings of the 47th AIAA Aerospace Sciences Meeting and Exhibit, 5-8 Jan. 2009, Orlando, Florida, AIAA 2009-0578.

Shyy, W., Jenkins, D. A., and Smith, R. W., 1997. Study of adaptive shape airfoils at low Reynolds number in oscillatory flows. AIAA Journal 35, 1545-1548.

Shyy, W., Berg, M., and Ljungqvist, D., 1999. Flapping and flexible wings for biological and micro air vehicles. Progress in Aerospace Sciences 35, 455-505.

Smith, R., and Shyy, W., 1995. Computational model of flexible membrane wings in steady laminar flow. AIAA Journal 33, 1769-1777.

Smith, R., and Shyy, W., 1996. Computation of aerodynamic coefficients for a flexible membrane airfoil in turbulent flow: a comparison with classical theory. Physics of Fluids 8, 3346-3353.

Song, A.J., and Breuer, K.S., 2007. Dynamics of a compliant membrane as related to mammalian flight. In: Proceedings of the 45th AIAA Aerospace Sciences Meeting and Exhibit, 8-11 Jan. 2007, Reno, Nevada, AIAA 2007-665.

Song, A., Tian, X., Israeli, E., Galvao, R., Bishop, K., Swartz, S., and Breuer, K., 2008. Aeromechanics of membrane wings with implications for animal flight. AIAA Journal 46, 2096-2106.

Taylor, G., Wang, Z., Vardaki, E., and Gursul, I., 2007. Lift enhancement over flexible nonslender delta wings. AIAA Journal 45, 2979-2993.

Wu, J.Z., Lu, X., Denny, A.G., Fan, M., and Wu, J.M., 1998. Post-stall flow control on an airfoil by local unsteady forcing. Journal of Fluid Mechanics 371, 21-58.

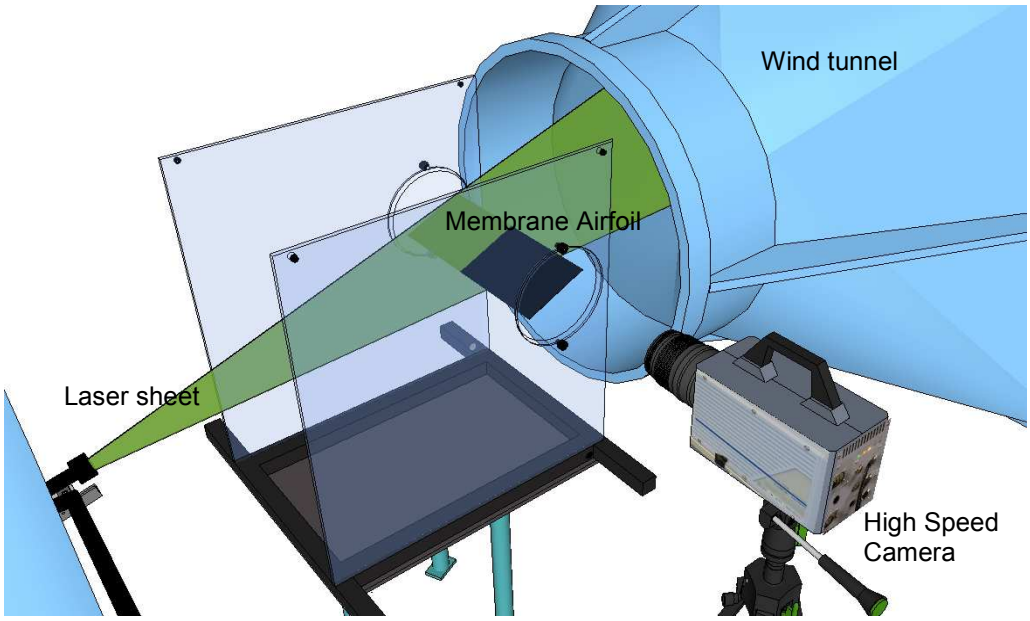

a)

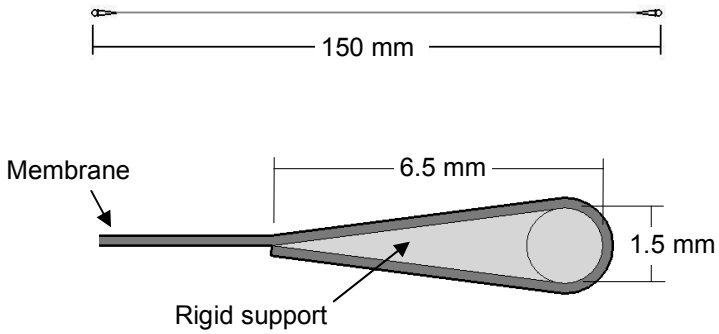

b)

Figure 1. a) Schematic of experimental setup; b) Cross-section of the membrane airfoil and details of leading- and trailing-edge.

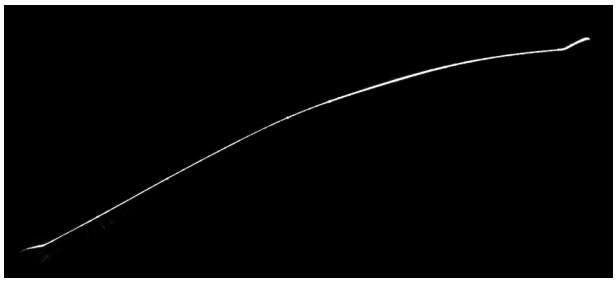

Figure 2. Membrane shape as obtained from the laser sheet visualization, $U_\infty = 5$ m/s, $\alpha = 20^o$.

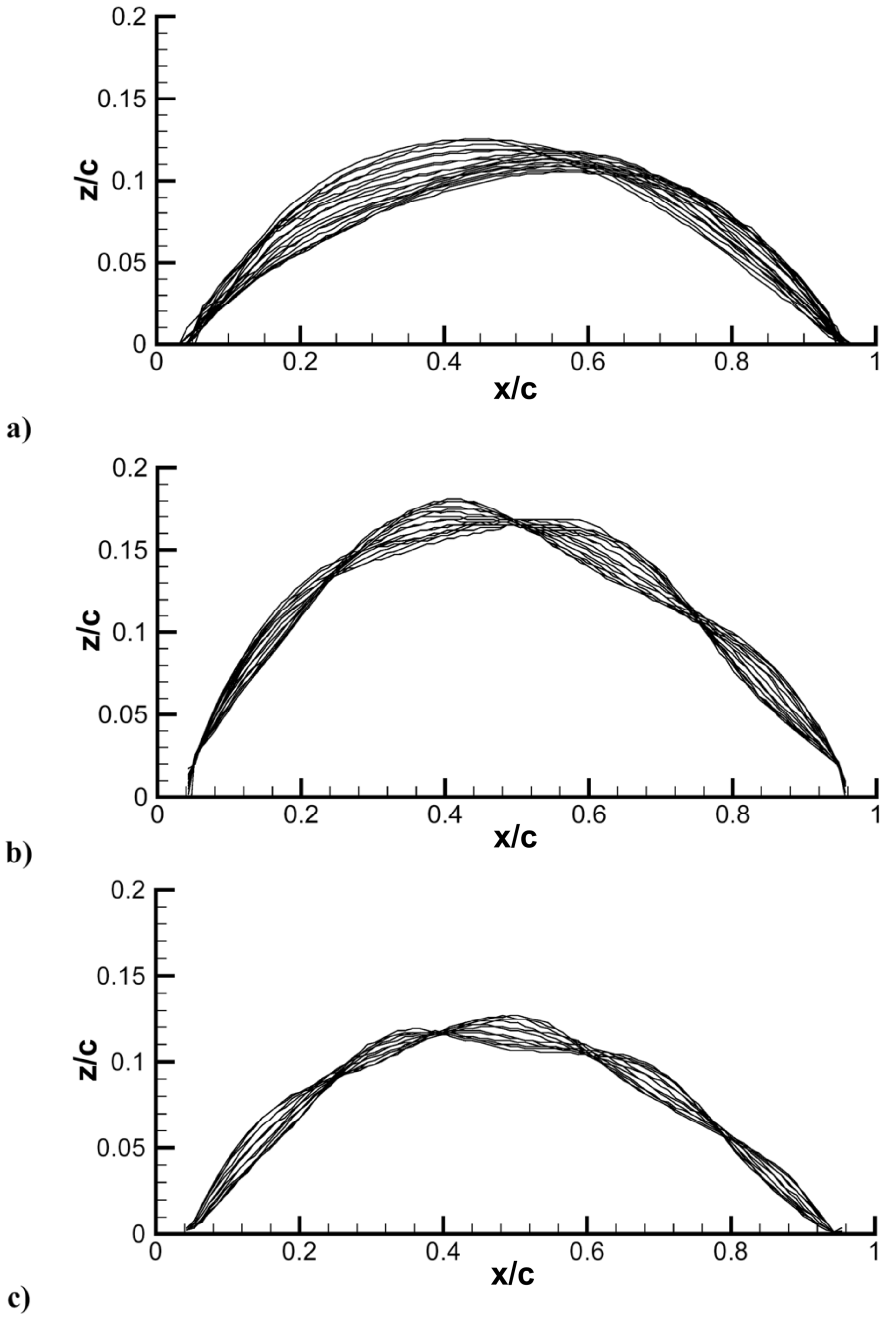

Figure 3. Digitized membrane shapes at different instants for U_∞ = 10 m/s for a) δ_0 = 0%, $\alpha = 25^o$; b) ε = 2.5%, $\alpha = 18^o$; c) δ = 0%, $\alpha = 13^o$.

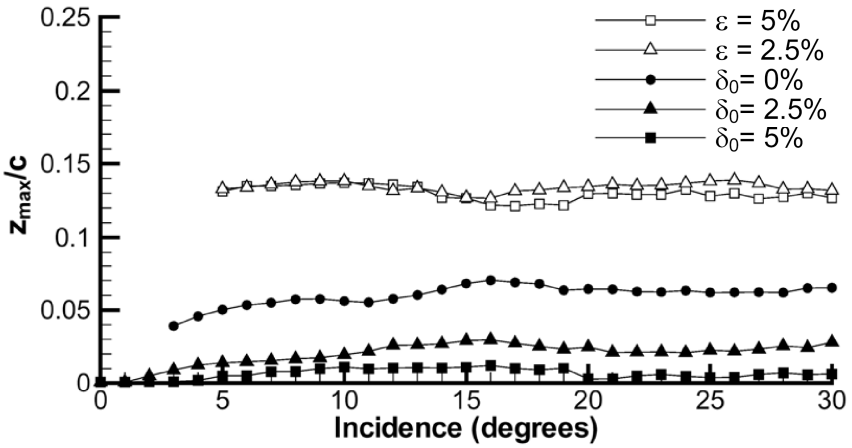

a)

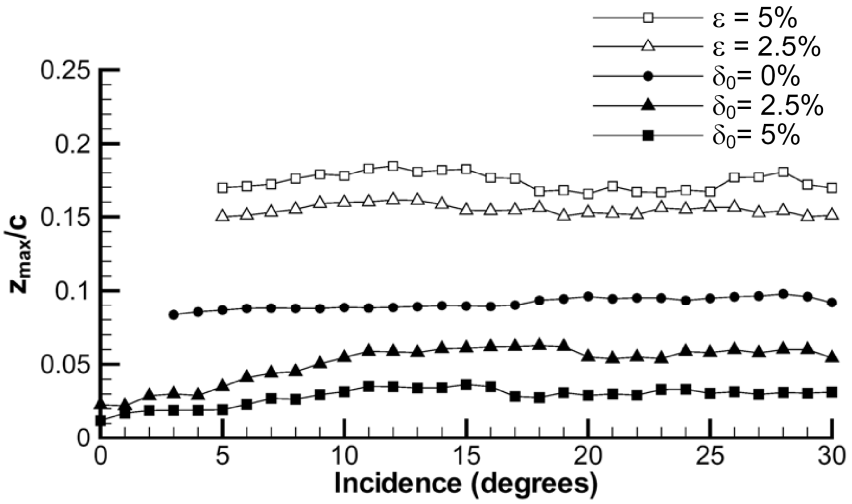

b)

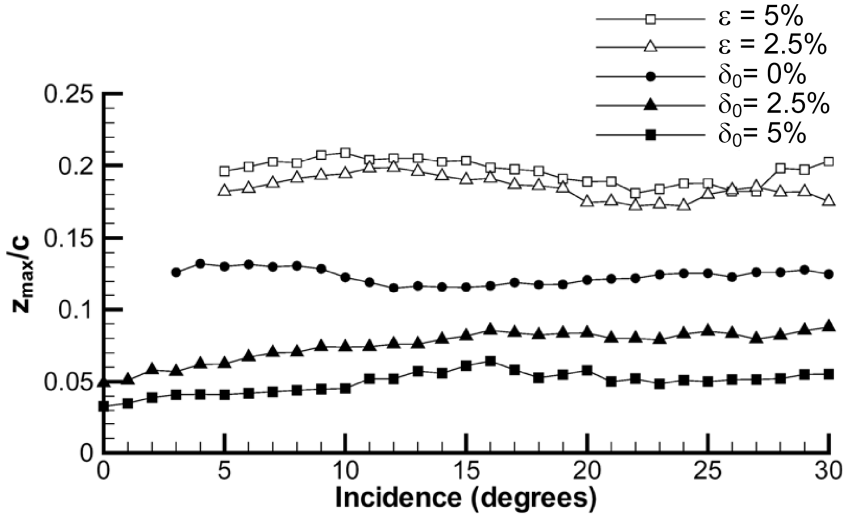

c)

Figure 4. Variation of maximum camber as a function of incidence for different pre-strains and excess lengths for a) U_∞ = 5 m/s; b) U_∞ = 7.5 m/s; c) U_∞ = 10 m/s.

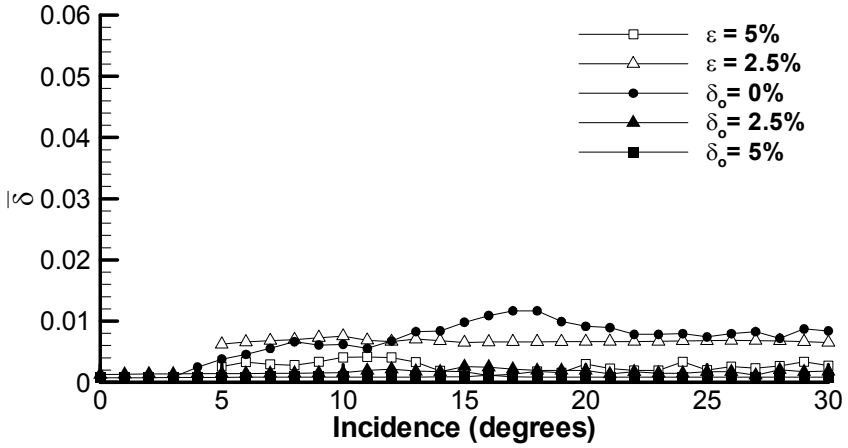

a)

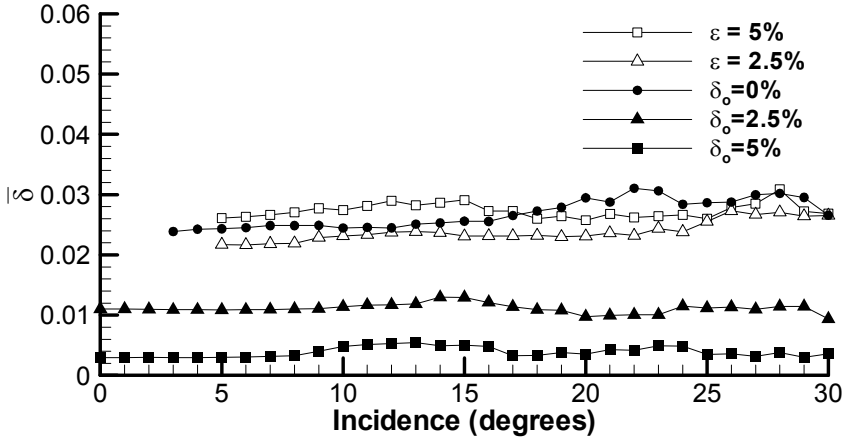

b)

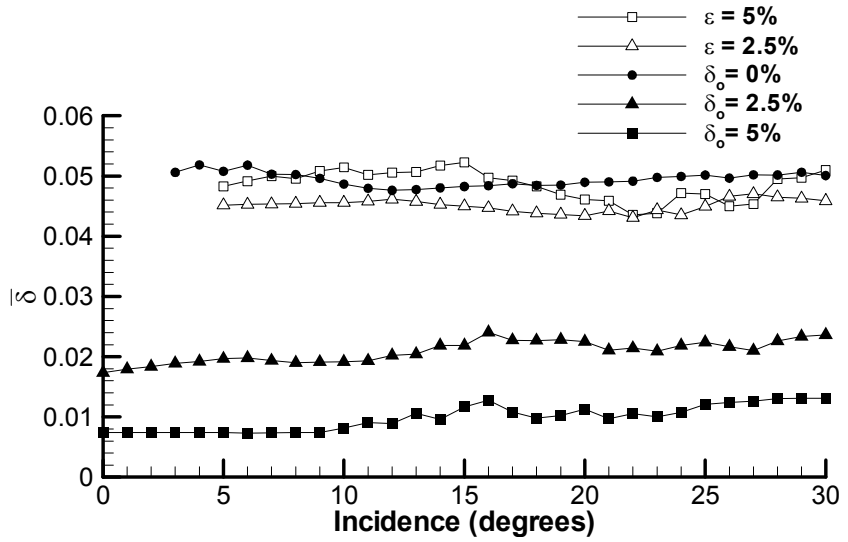

c)

Figure 5. Variation of time-averaged strain as a function of incidence for different pre-strains and excess lengths for a) $U_\infty = 5$ m/s; b) $U_\infty = 7.5$ m/s; c) $U_\infty = 10$ m/s.

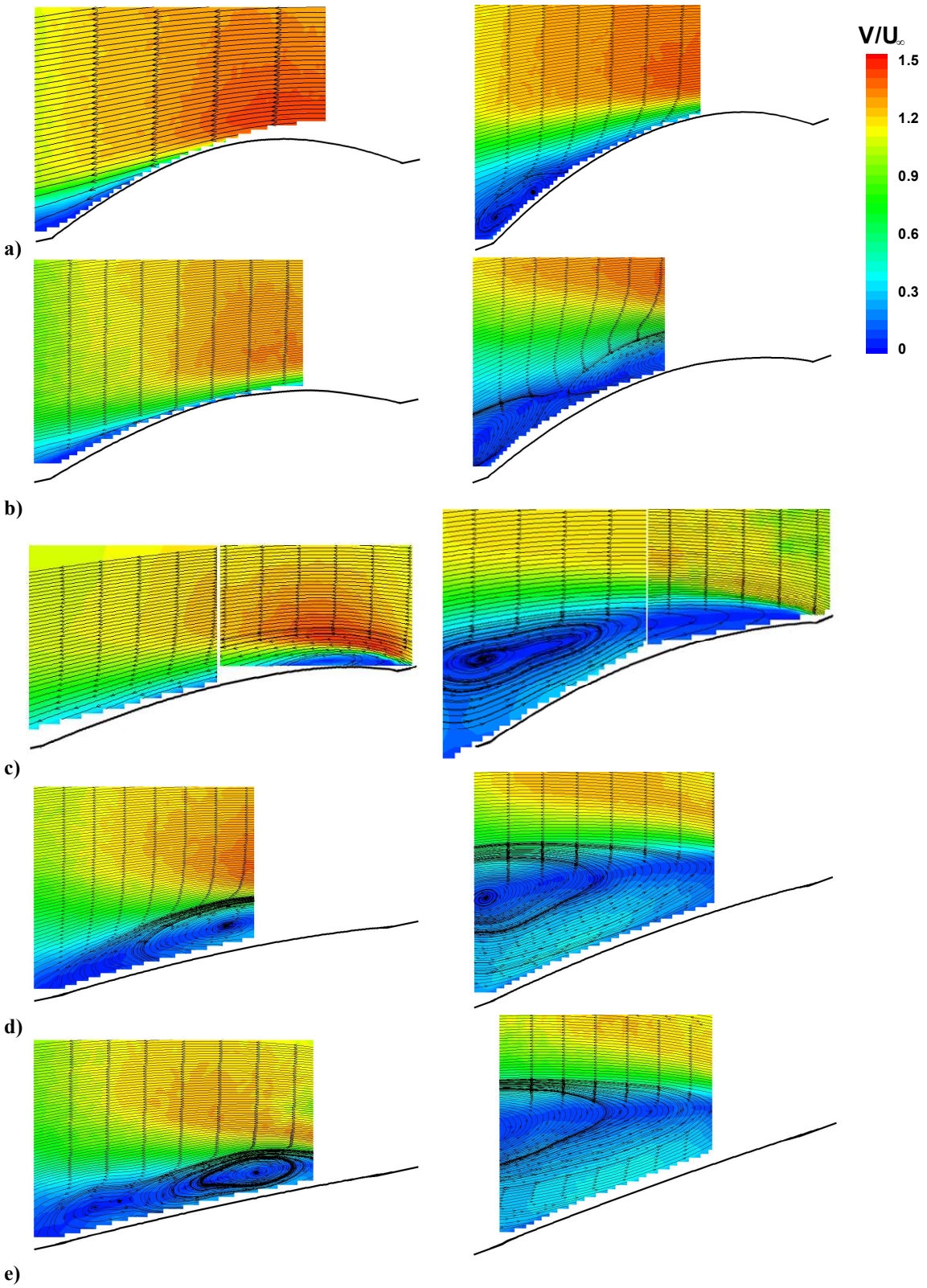

Figure 6. Magnitude of the time-averaged velocity and streamlines at U_∞ = 5 m/s (left: α = 12°, right: α = 20°) for a) ε = 5%; b) ε = 2.5%; c) δ = 0%; d) δ_0 = 2.5%%; e) δ_0 = 5%.

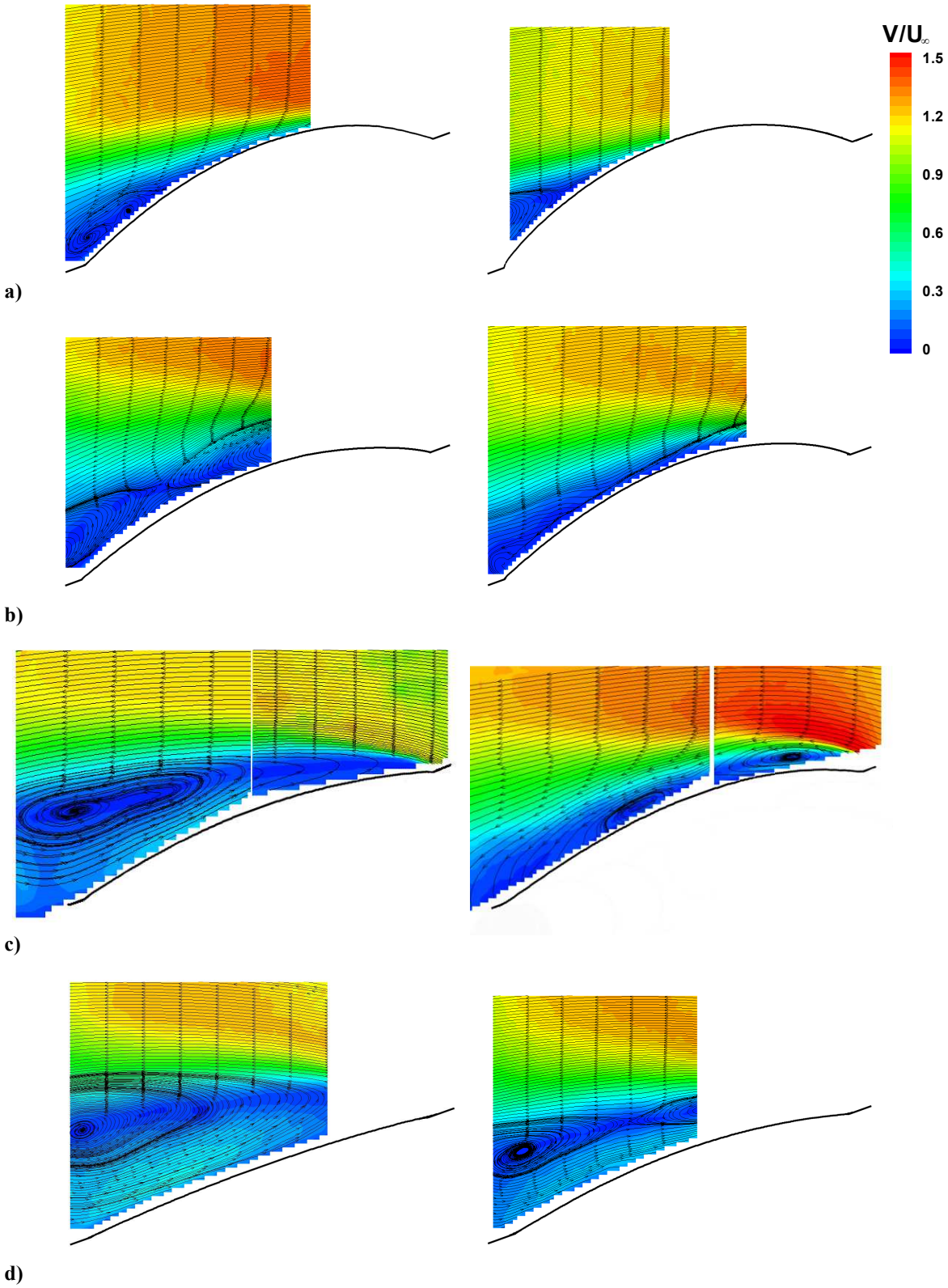

Figure 7. Magnitude of the time-averaged velocity and streamlines at $\alpha = 20^{o}$ (left: $U_{\infty} = 5$ m/s, right: $U_{\infty} = 7.5$ m/s) for a) $\varepsilon = 5\%$; b) $\varepsilon = 2.5\%$; c) $\delta = 0\%$; d) $\delta_0 = 2.5\%$.

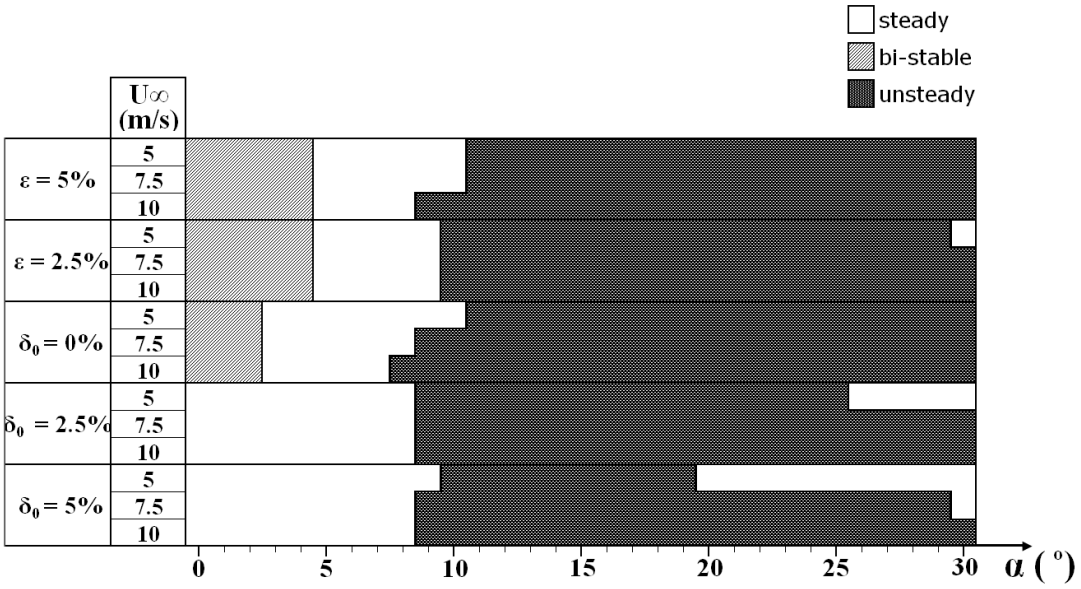

Figure 8. Membrane regimes as a function of incidence at different free stream velocities for different pre-strains and excess lengths.

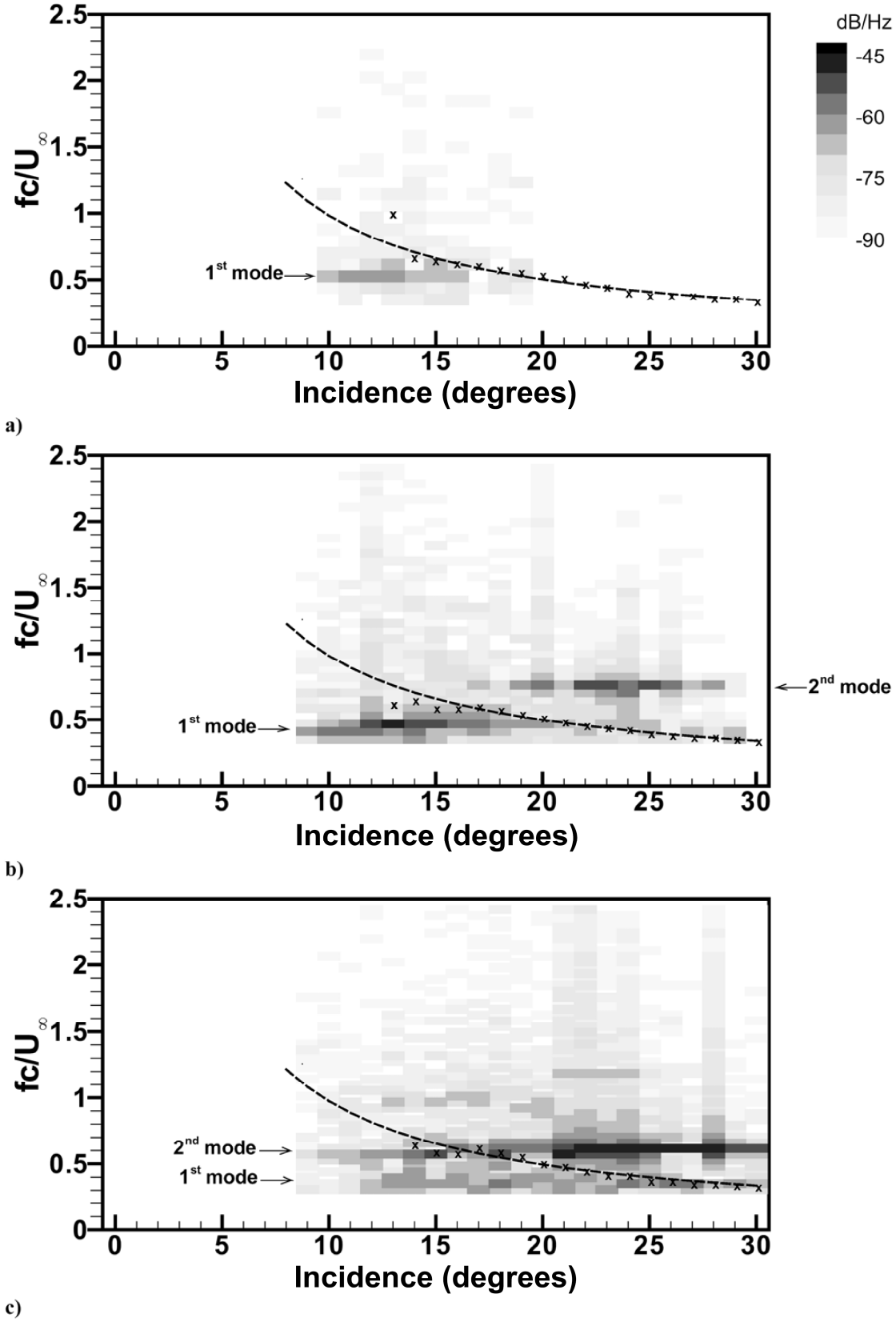

Figure 9. Power spectral density of membrane vibrations for δ_0 = 5% for a) U_∞ = 5 m/s; b) U_∞ = 7.5 m/s; c) U_∞ = 10 m/s.

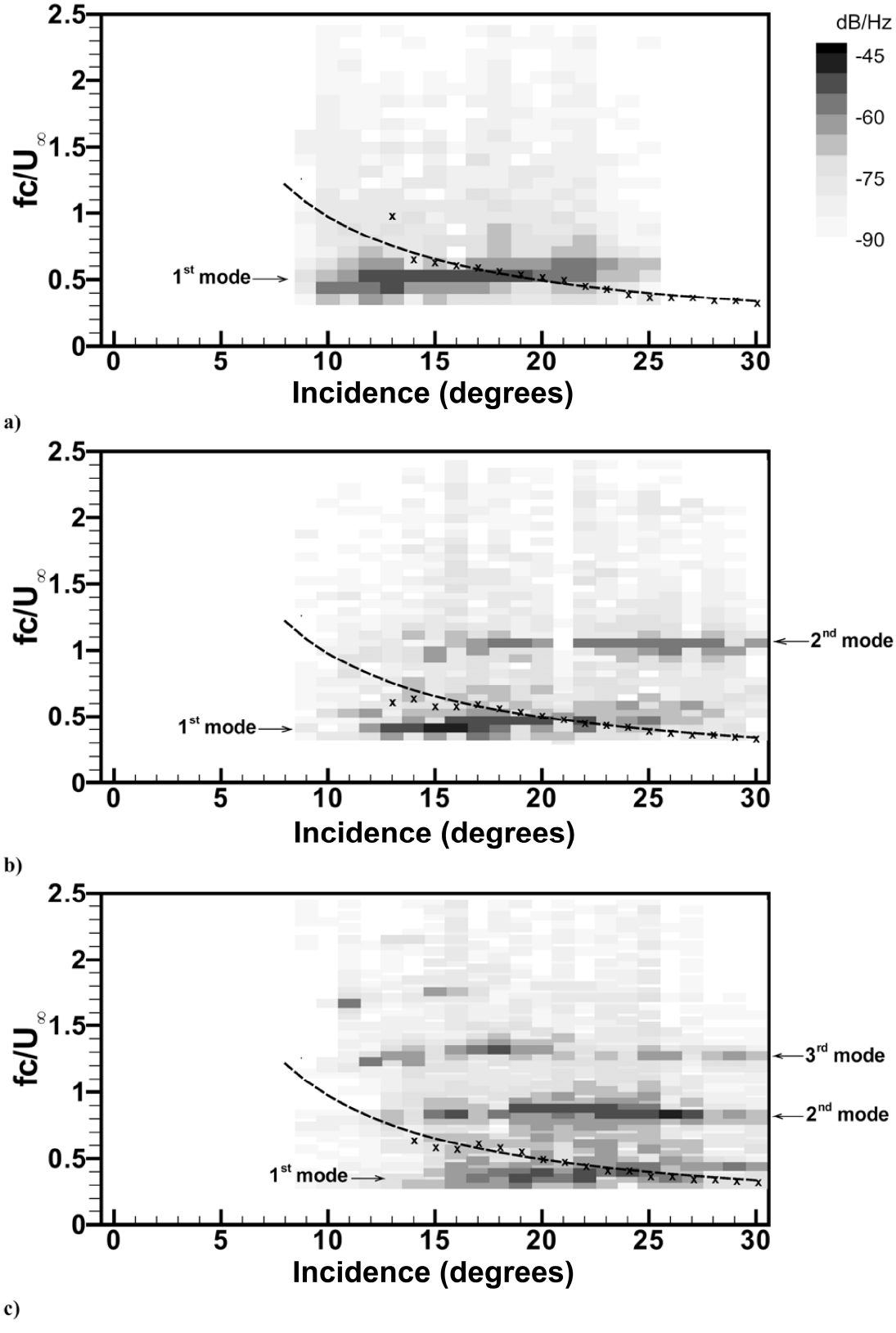

Figure 10. Power spectral density of membrane vibrations for δ_0 = 2.5% for a) U_∞ = 5 m/s; b) U_∞ = 7.5 m/s; c) U_∞ = 10 m/s.

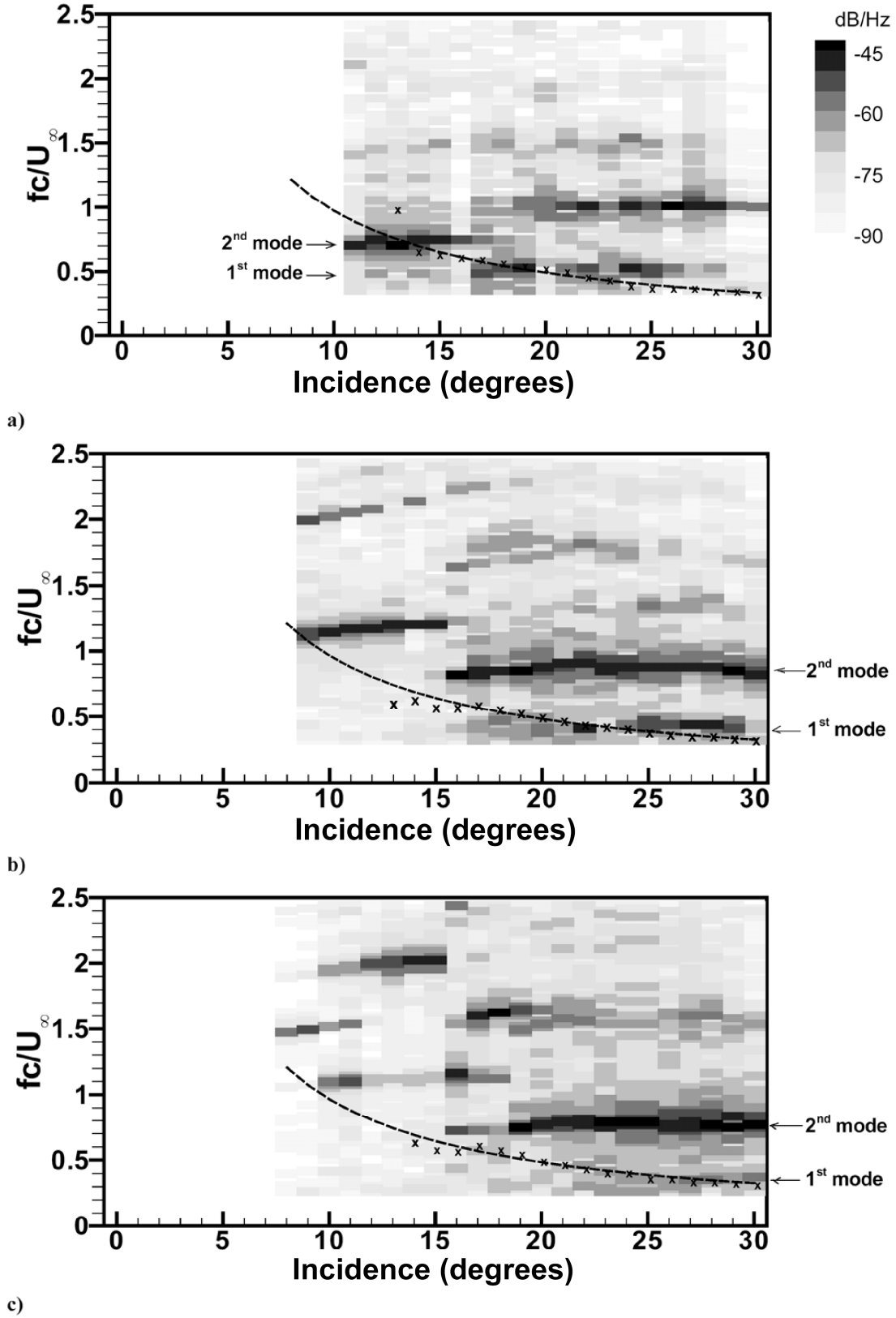

Figure 11. Power spectral density of membrane vibrations for δ_0 = 0% for a) U_∞ = 5 m/s; b) U_∞ = 7.5 m/s; c) U_∞ = 10 m/s.

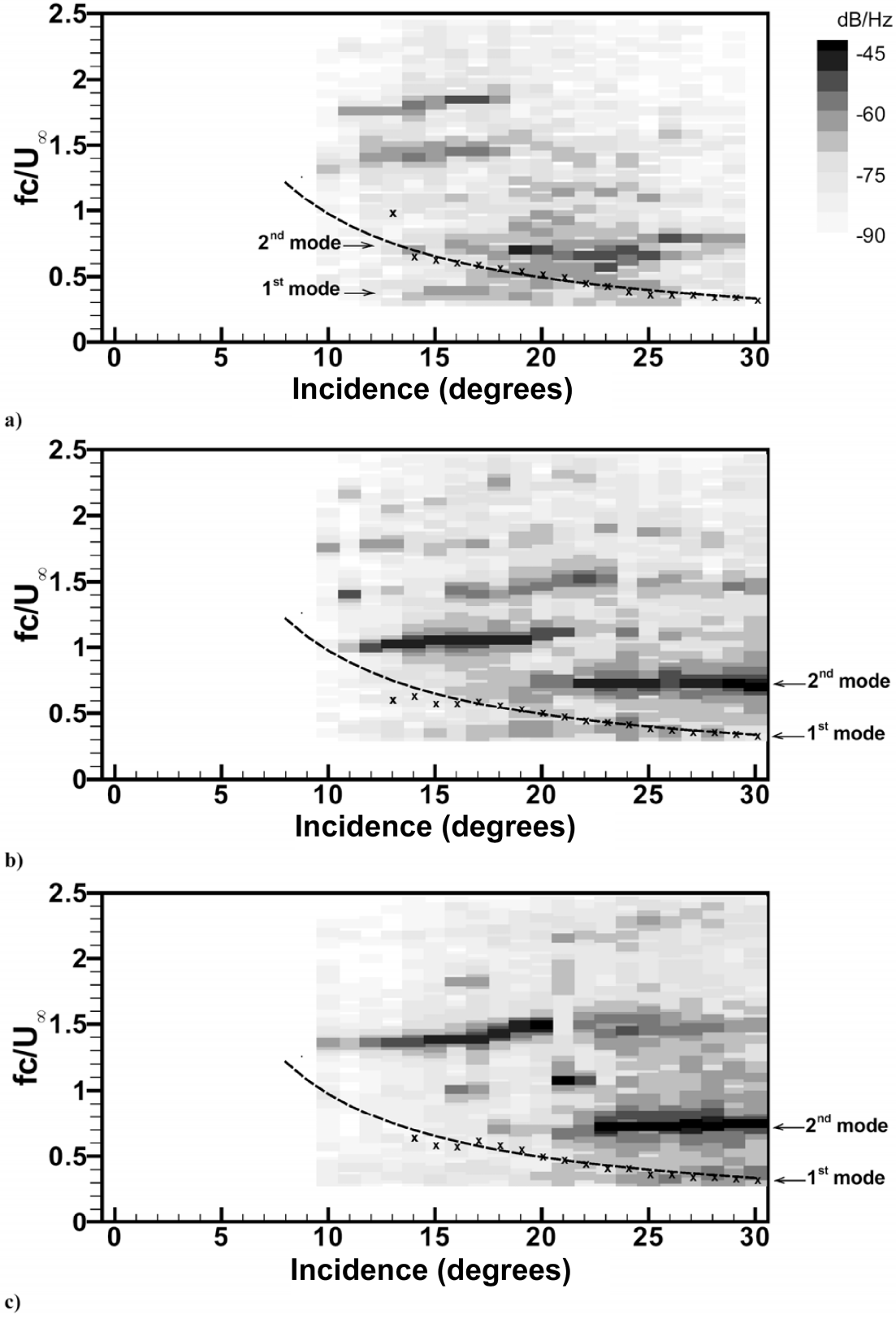

Figure 12. Power spectral density of membrane vibrations for ε = 2.5% for a) U_∞ = 5 m/s; b) U_∞ = 7.5 m/s; c) U_∞ = 10 m/s.

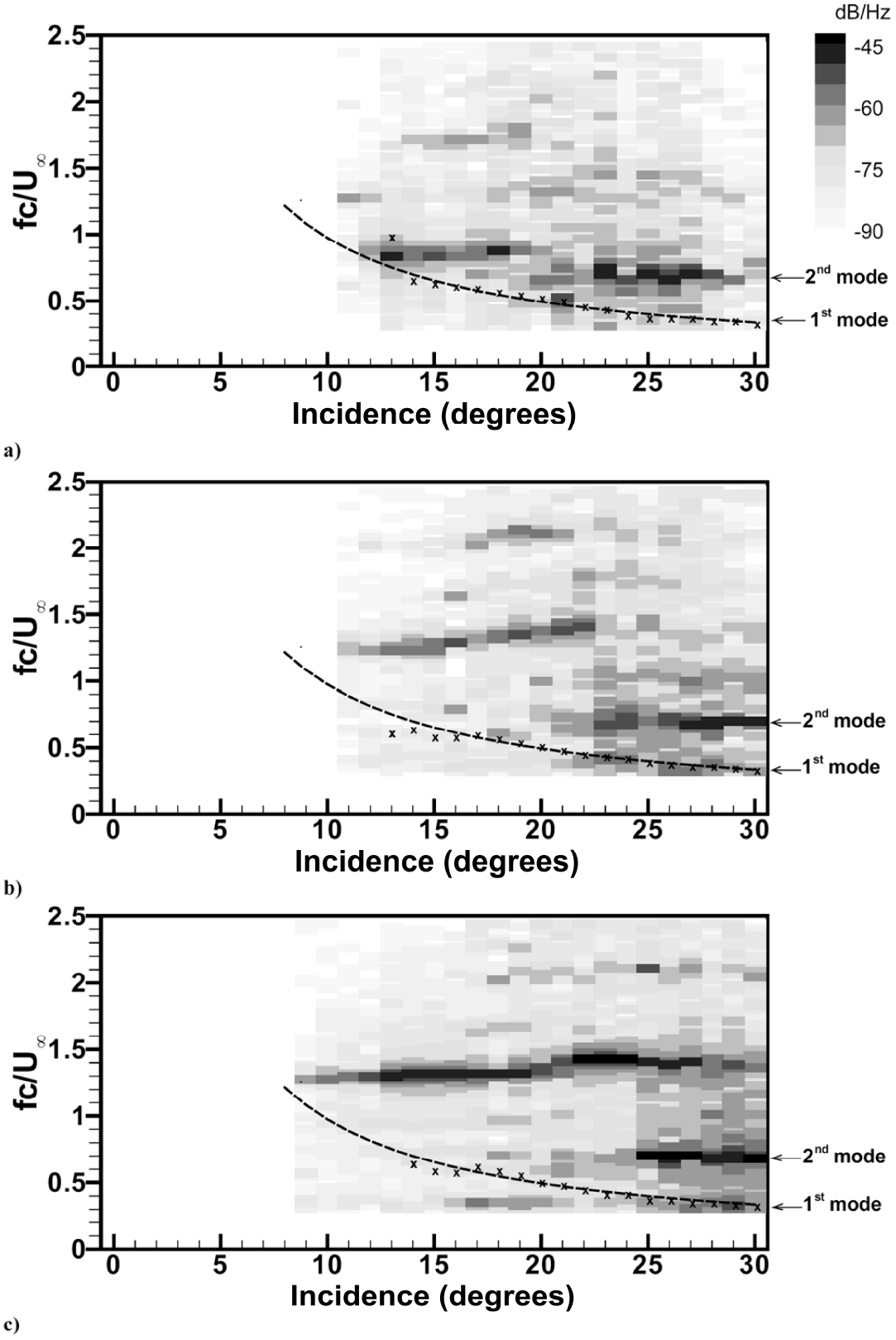

Figure 13. Power spectral density of membrane vibrations for ε = 5% for a) U_∞ = 5 m/s; b) U_∞ = 7.5 m/s; c) U_∞ = 10 m/s.

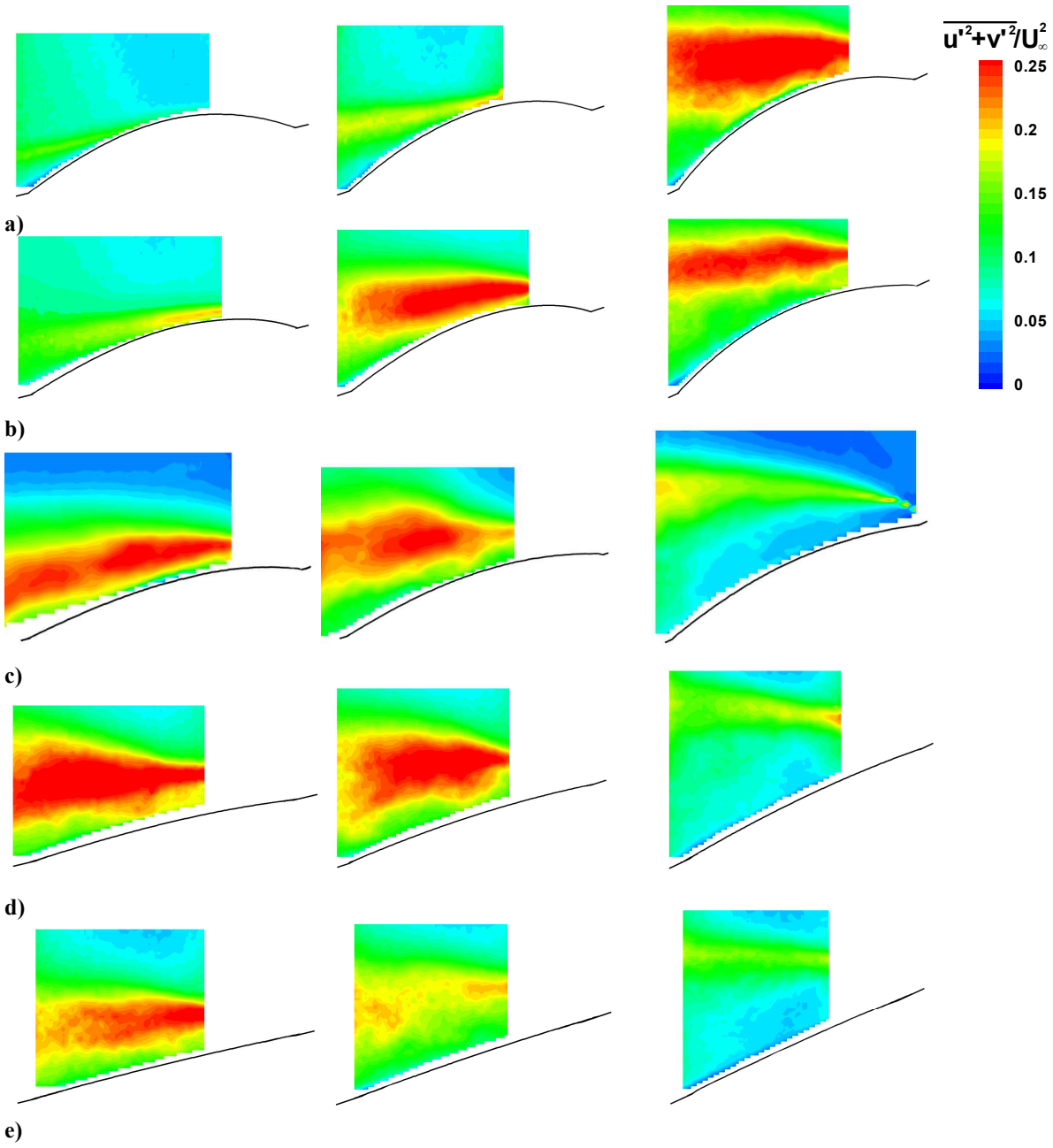

Figure 14. Turbulence intensity at U_∞ = 5 m/s (left: α = 14°, middle: α = 18° right: α = 25°) for a) ε = 5%; b) ε = 2.5%; c) δ = 0%; d) δ_0 = 2.5%; e) δ_0 = 5%.

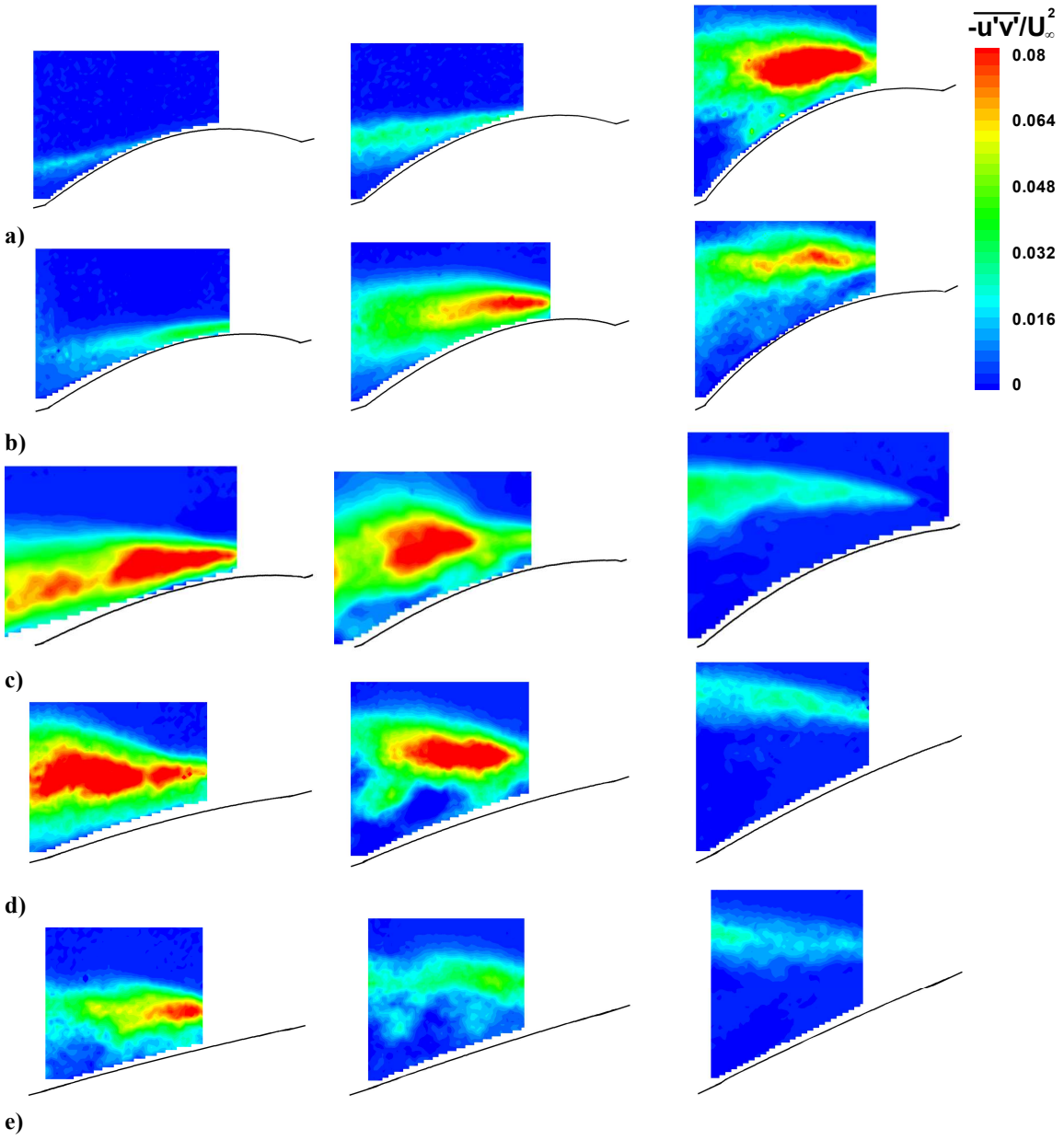

Figure 15. Reynolds stress at U_∞ = 5 m/s (left: α = 14°, middle: α = 18° right: α = 25°) for a) ε = 5%; b) ε = 2.5%; c) δ = 0%; d) δ_0 = 2.5%; e) δ_0 = 5%.

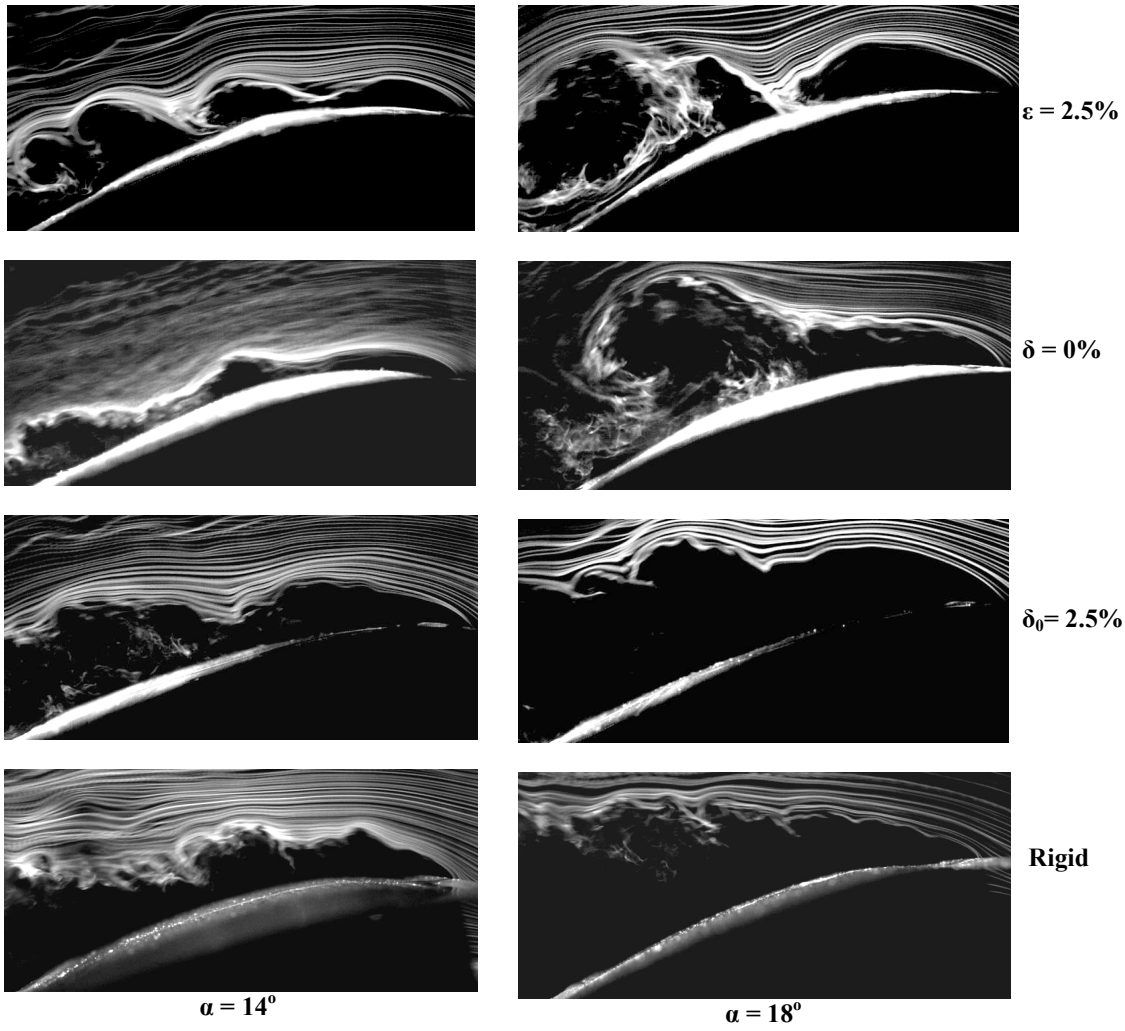

Figure 16. Smoke flow visualization for flexible (ε = 2.5%, δ = 0%, and δ_0 = 2.5%) and rigid wings, U_∞ = 5 m/s, (left: α = 14°, right: α = 18°).